ChemElectroChem

Research Article
doi.org/10.1002/celc.202400707

Chemistry Europe
European Chemical Societies Publishing

www.chemelectrochem.org

VIP *Very Important Paper*

Probing the Properties of Locally Formed Solid Electrolyte Interphases on Hard Carbon Anodes

Salimeh Saleh,[a] Sven Daboss,[a] Tom Philipp,[a] David Schäfer,[b] Marcus Rohnke,[b] and Christine Kranz*[a]

The solid electrolyte interphase (SEI) formation on hard carbon (HC), as one of the most widely used anode materials in sodium (Na)-ion batteries, is still not fully understood compared to the SEI formation on anodes used in lithium (Li)-ion batteries, in terms of passivation properties and stability, which strongly depends on various factors such as experimental parameters and the electrolyte composition. Herein, we report the localized formation of SEI microspots on HC using cyclic voltammetry in combination with scanning electrochemical cell microscopy (SECCM) in non-aqueous ether- and carbonate-based electrolytes. Using the same instrumental setup for SECCM and for atomic force microscopy (AFM), the locally formed SEI spots could be directly characterized with respect to the morphology, height, passivation and nanomechanical properties in dependence of the experimental deposition parameters such as scan rate and cycling number. In addition, time-of-flight secondary ion mass spectrometry (ToF-SIMS) in combination with AFM revealed the chemical composition of the SEI layer by recording spatially resolved 3D mass maps of the SEI spots. This combination of high-resolution microscopic and spectrometric methods provides new insights into the dynamics of SEI formation as a function of the electrolyte and the experimental parameters.

Introduction

Since the introduction of the concept of the solid electrolyte interphase (SEI) as an ionically conducting, electrically insulating layer by Peled in the late 1970s, several SEI models have evolved over the past decades.[1] The "mosaic model", which redefined the SEI model as a heterogeneous structure of organic and inorganic phases, recognizing its non-uniform, complex nature and the impact of its composition on ionic conductivity and stability under cycling conditions[2] and the "layered model" which describes the SEI as multiple layers, each with distinct compositions and function, which collectively influence battery performance through different mechanical and ionic properties.[3–5] The recently established "dynamic SEI model" accounts for the formation, dissolution, and swelling processes of the SEI layer under different electrochemical conditions over time.[6–9]

To date, the SEI layer formation has been mainly studied for lithium-ion batteries (LIBs)[10–12] (and references therein). With the commercialization of sodium-ion batteries (SIBs), as more sustainable and cost-effective alternative solutions for energy storage, the understanding of the SEI formation, its dynamic behavior and its composition is crucial.[13–15] Hard carbon (HC) is one of the most widely used anode materials for SIBs due to its excellent storage capacity for sodium ions, the low operating voltage, its high reversible specific capacity, high conductivity and the low cost.[16–18] A previous study has shown significantly different lifetimes for cells using HC, which is likely attributed to differences in the electrolyte used, the mass loading of the electrode with the active material, the C-rates, or other experimental conditions.[19] The complex morphology of HC, governed e.g. by the initial renewable bio-resources, the manufacturing processes and the electrochemical dynamics of sodium intercalation, poses new challenges for the SEI formed on HC.[20,21] Currently, two models are discussed: the adsorption-intercalation-filling model, which is related to Na^+ adsorption at defects and intercalation of Na^+ between expanded layers (reflected by the high-voltage sloping region (2.0 V–0.1 V vs Na/ Na^+)) followed by pore filling with Na at potentials below 0.1 V vs Na/ Na^+ (plateau region).[22,23] Alternatively, the adsorption-filling[24] or adsorption-intercalation model are discussed, which again are based on the adsorption of Na^+ at high potentials, followed by either filling of the pores with Na or intercalation of Na^+.[25] During the first charging cycle within the high potential region, irreversible reactions such as decomposition of the electrolyte lead to the formation of the SEI.

The composition, stability and morphology of the SEI are strongly influenced by parameters such as the electrolyte salt (mainly sodium perchlorate ($NaClO_4$), sodium hexafluorophosphate ($NaPF_6$), and sodium bis(trifluoromethylsulfonyl)imide (NaTFSI)), the solvent (mainly carbonate-based or ether-based), and the presence of additives (e.g., fluoroethylene carbonate

[a] Dr. S. Saleh, Dr. S. Daboss, T. Philipp, Prof. Dr. C. Kranz
Institute of Analytical and Bioanalytical Chemistry (IABC)
Ulm University, Albert-Einstein-Allee 11, 89081 Ulm (Germany)
E-mail: christine.kranz@uni-ulm.de

[b] D. Schäfer, Prof. Dr. M. Rohnke
Institute of Physical Chemistry and Center for Materials Research
Justus Liebig University Giessen, Heinrich-Buff-Ring 17, 35392 Giessen (Germany)

Supporting information for this article is available on the WWW under https://doi.org/10.1002/celc.202400707

(FEC) and vinyl carbonate (VC)). The mechanism of the SEI formation on HC and its composition in dependence of the electrolyte used has been intensively studied during the last decades, as the higher solubility of the SEI leads to self-discharge of the cell and further electrolyte decomposition, resulting in low Coulombic efficiencies.[26–28]

Similar to the SEI formed on graphite, also for HC composite anodes, the formation of a uniform SEI is required to prevent ongoing electrolyte decomposition, to minimize rapid capacity loss, and to block electrons to minimize the battery self-discharge. Recent studies have reported that the SEI layer in SIBs is typically thicker and more inhomogeneous compared to LIBs, leading to frequent dissolution and instability during cycling.[9,29,30] The SEI formation on HC in SIBs using carbonate- and ether-based electrolytes depends on the electrolyte composition, cycling conditions, possible side reactions, and the structural properties of the electrode materials, among other factors.[15,31,32] Understanding these mechanisms is critical for optimizing the performance of SIBs. The mechanism of SEI formation and their properties are still controversially debated in the literature, especially for ether-based electrolytes, e.g., $NaPF_6$ in 1-methoxy-2-(2-methoxyethoxy) ethane (usually abbreviated as diglyme), as some studies have linked rapid capacity fading to an unstable SEI layer, while others have reported the presence of a beneficial thin SEI layer or even the absence of an SEI on HC.[33–35] More recently, diglyme has been shown to facilitate the formation of a thin SEI with low internal resistance on HC anodes (vs Na/Na^+) in 1 M $NaPF_6$.[33–35] The surface species and the chemical composition of the SEI on HC has been studied with methods such as X-ray photoelectron spectroscopy (XPS) and time-of-flight secondary ion mass spectrometry (ToF-SIMS).[36,37] Nanoscale imaging techniques, such as scanning electron microscopy (SEM) and transmission electron microscopy (TEM), have been used to obtain information on the thickness and the morphological heterogeneity of the SEI. These tools have revealed the SEI's complex structural variations and dynamic behavior over time, essential for understanding how the SEI affects the battery lifespan and electrochemical performance.[38–41] However, significant challenges remain in SEI characterization. High-resolution techniques often suffer from required transfer of the samples from an inert environment to the analytical instrument. This can compromise the ability to fully protect the SEI from exposure to air, which can alter or damage its delicate composition.

Scanning probe microscopy (SPM) techniques have recently gained attention for non-destructive, high-resolution analysis of sensitive interphases, such as the SEI layer.[42,43] Among these, atomic force microscopy (AFM) is a powerful method for mapping surface topography, determining heterogeneities in nanomechanical properties, and mapping local conductivity. Nanoscale surface changes at battery electrodes have been extensively studied using AFM[44,45] and related techniques, such as force spectroscopy,[46–48] electrochemical strain microscopy (ESM),[49] and electrochemical (ec-)AFM.[50–52] Several studies have focused on the determination of nanomechanical properties of the SEI using AFM force spectroscopy to analyze the morphology and Young's modulus of SEI films formed on manganese oxide (MnO) anodes,[47] silicon,[53] solid-state lithium batteries[54] or at graphite anodes.[55] Furthermore, *in situ* studies allow real-time observation of the SEI formation as recently demonstrated for highly oriented pyrolytic graphite (HOPG),[56] graphite and HC,[52] thus contributing to a deeper understanding of the interphase properties critical for improving battery performance.[43,57]

Within the last decade, scanning electrochemical cell microscopy (SECCM), an SPM technique that uses a nano- or micropipette to create a localized electrochemical droplet cell, has been applied to battery research. When combined with techniques such as cyclic voltammetry (CV), SECCM allows comprehensive electrochemical investigation of the SEI under different conditions while minimizing the risk of surface contamination. SECCM has been demonstrated to visualize lithium-ion intercalation at lithium iron phosphate ($LiFePO_4$) cathodes[56] and facet-dependent diffusion of Li-ions at $Li_4Ti_5O_{12}$ (LTO) thin film electrodes.[58] Unwin and coworkers have shown that SECCM can be used for local formation of a SEI layer on model electrodes (HOPG) in an inert glovebox atmosphere. Their studies were focused on different grades of HOPG characterized by different grades of structural defects that influence the properties of the formed SEI.[59]

In this study, we used SECCM in combination with CV to form SEI microspots on selected embedded and polished HC composite electrodes. Using SECCM, SEI microspots were deposited on individual HC particles in two different electrolytes: 1 M $NaPF_6$ in EC/PC = 1 : 1 (w/w) solution and 1 M $NaPF_6$ in diglyme. Using an SPM instrument, capable of switching from SECCM mode to AFM, these spots could be directly characterized by AFM, conductive (c)-AFM, and non-contact AFM to visualize the size, height, morphology, the insulating nature and the nanomechanical properties of the formed SEI as a function of the used electrolyte and number of cycles. Additional AFM-ToF-SIMS measurements provide information on the chemical composition of the SEI microspots.

Results and Discussion

Formation of SEI Microspots

Figure 1a shows the scheme of the local SEI formation on a HC particle using SECCM in the two different electrolytes, carbonate-based or ether-based using $NaPF_6$. The AFM instrument, which is also equipped with a scan head to perform scanning ion conductance microscopy (SICM) or SECCM experiments is located in an argon-filled glovebox to maintain an inert environment. For the presented studies, a micropipette with an approximate pipette opening of 1 μm in diameter (see Figure S1) was used as the electrochemical probe. This pipette was filled with either 1 M $NaPF_6$ in EC/PC (1 : 1) + 5 wt% FEC or 1 M $NaPF_6$ in diglyme. As a reference electrode, a copper wire (diameter = 200 μm) was coated with sodium by electroplating, which then served as the Na reference electrode that is located inside the pipette. To avoid artifacts induced by the morphology of the HC composite electrodes, they were embedded in

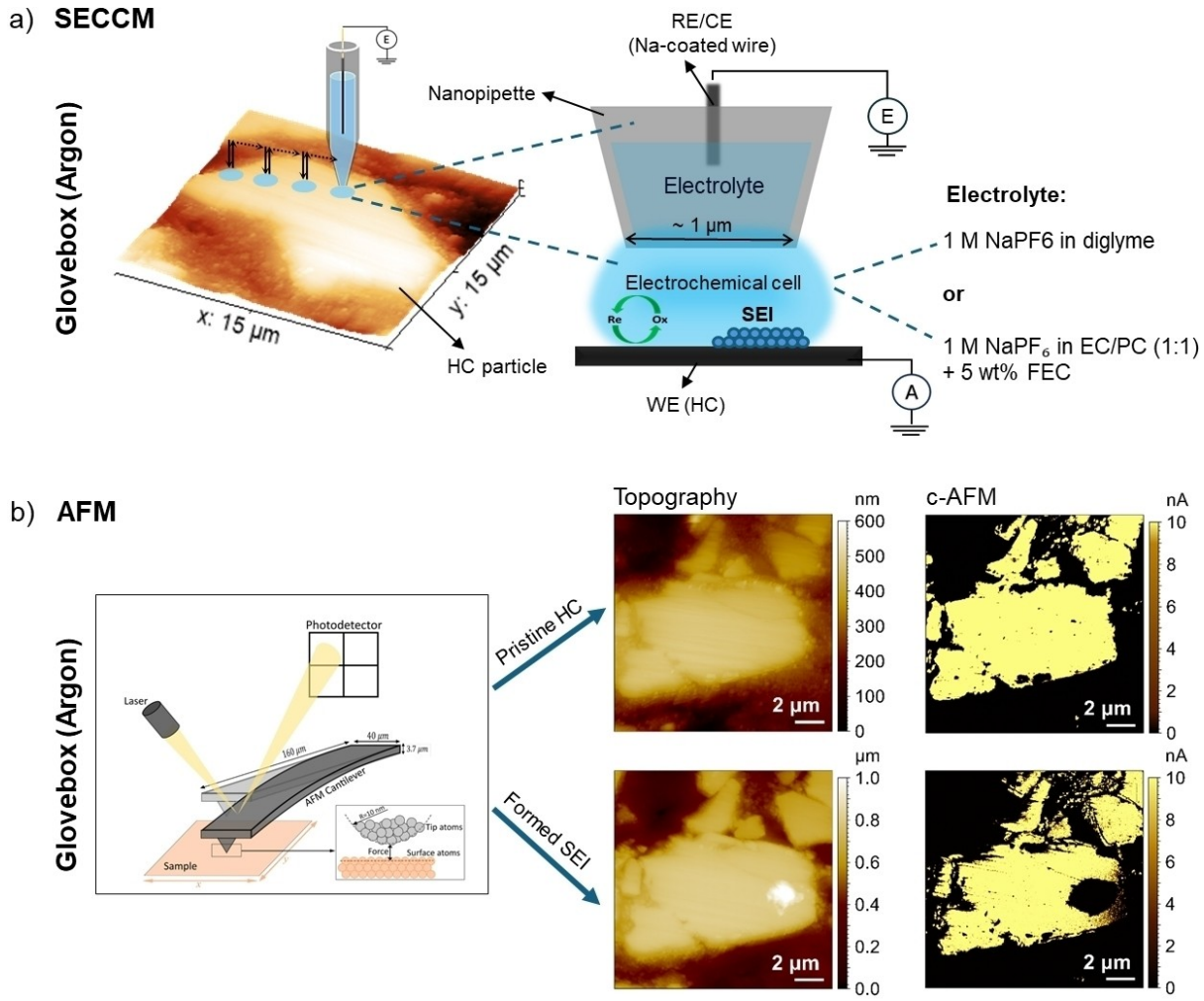

Figure 1. (a) Schematic of the SECCM setup in an argon-filled glovebox, illustrating a single-barrel pipette filled with electrolyte, making a localized electrochemical droplet cell on the polished HC surface. (b) AFM and c-AFM images showing the pristine HC particle surface, and the droplet footprint left after the SECCM test of 1 charge-discharge cycle in 1 M $NaPF_6$ in EC/PC (1 : 1) + 5 wt% FEC. The topography and c-AFM maps of the droplet footprint reveal details about the SEI layer morphology and its insulating properties.

epoxy resin and polished as previously reported.[43,52] The surface roughness (Sa) was reduced from 1.85 µm ± 0.19 µm (non-embedded) to 0.14 µm ± 0.04 µm (embedded and polished) (n = 5). The pipette was approached toward the polished HC particle surface by monitoring the ion current. A sudden change (or "jump") in the ion current indicated contact between the droplet and the surface, producing a stable liquid meniscus between the pipette and the HC surface (see Figure S2). Once this meniscus was formed, CV was performed for localized charge-discharge cycling experiments under varying electrochemical conditions (like scan rate and cycling number). After rinsing the sample in the AFM electrochemical cell carefully with dimethyl carbonate (DMC) three times, AFM and c-AFM images were recorded in argon atmosphere on the single polished HC particle prior and after cycling (1 mV/s scan rate, 2.0 V to −0.2 V vs Na/Na^+ in 1 M $NaPF_6$ in EC/PC (1 : 1) + 5 wt% FEC), which are shown in Figure 1b.

The AFM images in Figure 1b show the topography and conductivity of the pristine HC particle, along with the distinct footprint of the SEI, which is evident from the morphology of the spot and the blocking behavior reflected by the current drop in the c-AFM data. The well-defined and consistent electrolyte footprint generated by the SECCM probe's meniscus suggests that the meniscus remained stable under the selected experimental conditions.

Figures 2a and b show localized SEI layers on a single HC particle formed by SECCM in 1 M $NaPF_6$ in EC/PC (1 : 1) + 5 wt% FEC electrolyte. The pipette was moved in hopping mode to different locations on the same HC particle and CV was performed in a potential range from 2.0 V to 0.001 V or 2.0 V to −0.2 V vs Na/Na^+, respectively. The scan rate and cycling number were varied as follows for the different spots indicated by the numbers (see Figure 2b): spot 1: 1 cycle, 0.5 mV/s, 2.0 V to 0.0 V vs Na/Na^+; spot 2: 1 cycle, 1 mV/s, 2.0 V to −0.2 V vs Na/Na^+; spot 3: 1 cycle, 1 mV/s, 2.0 V to −0.2 V vs Na/Na^+; spot 4: 1 cycle, 0.1 mV/s, 2.0 V to −0.2 V vs Na/Na^+; spot 5: 3 cycles, 0.1 mV/s, 2.0 V to −0.2 V vs Na/Na^+; spot 6: 1 cycle, 5 mV/s, 2.0 V to −0.2 V vs Na/Na^+). It is evident from the topography

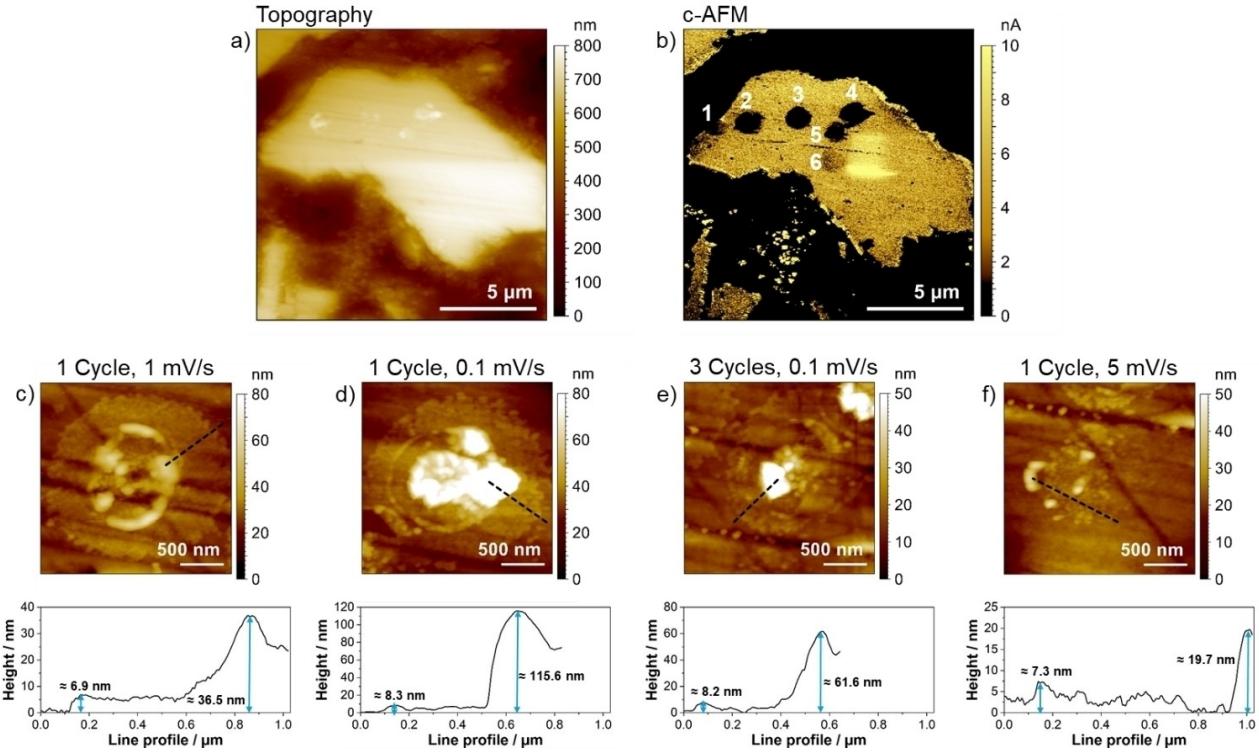

Figure 2. (a) Topographic AFM image of the HC particle showing the footprint of electrolyte deposition following the SECCM test. (b) c-AFM image of the same area, highlighting conductive and insulating regions. (c–f) Higher-magnification topographic images of the formed SEI spots visible in (a) under different electrochemical cycling conditions: (c) 1 cycle at 1 mV/s (spot 3 in Figure 2b), (d) 1 cycle at 0.1 mV/s (spot 4 in Figure 2b), (e) 3 cycles at 0.1 mV/s (spot 5 in Figure 2b), and (f) 1 cycle at 5 mV/s (spot 6 in Figure 2b). Line profiles below each image show the height changes along the black dashed lines, illustrating the observed heights influenced by cycling conditions.

image that the spot 1 and spot 6 are not visible in the AFM topography image, as spot 1 is at the edge of the HC particle and spot 6 seems to be too thin to be visible in the AFM topography image. The spot size of the formed localized SEI layers with 1.0 µm–1.4 µm corresponds well with the orifice size of the used micropipette. The c-AFM map in Figure 2b reveals the change in electronic conductivity of the HC particle after depositing the SEI microspots under different experimental conditions in $NaPF_6$ in EC/PC electrolyte with a clear contrast between the conductive pristine areas and the insulating SEI-covered regions. The SEI-covered areas show significantly reduced conductivity, reflecting the formation of an electronically insulating layer during the initial charge-discharge cycle. For spots 2–5 the conductivity drops almost to zero, whereas interestingly, spot 1 and 6, which are not visible in the topography image, also show a partial blocking of the conductive HC. The difference in the measured current between pristine HC particles and particles with a SEI in the c-AFM images exhibits a reduction of 58% for spot 1, and 60%, 60%, 62%, 56%, and 22% for spots 2, 3, 4, 5, and 6, respectively. The zoomed view of the topography maps of individual SEI microspots (3-6) are presented in Figures 2c–f. It is evident from the associated line scans that the SEI forms a uniform, thin layer with a thickness of approximately 6–8 nm. The observed thickness range is slightly lower but generally in agreement with the ex-situ measurements of the SEI formed in carbonate-based electrolytes reported by Lee et al.,[60] who observed SEI thicknesses of 10–20 nm using field emission transmission electron microscopy (FE-TEM) and XPS depth profiling. Although, it should be noted that the HC was sourced from a different commercial manufacturer and that the experimental conditions were not the same as used here.

A thin, uniform layer is covered by more heterogeneous depositions, with an average thickness of 58 ± 36 nm ($n = 4$). The formation of this heterogenous SEI structure is associated with the electrolyte decomposition during the first charge-discharge cycle. The presence of these two sub-layers may be related to the influence of the droplet curvature and with that on the local concentration gradients. Such curvature effects could promote the formation of spatially distinct layers with varying thicknesses. To investigate if this heterogeneity in layer thickness is related to the EC/PC solvent, SEI microspots were also deposited using an ether-based electrolyte, 1 M $NaPF_6$ in diglyme. Figures 3a and b show the topography and c-AFM maps of a SEI microspot deposited on a HC particle. The c-AFM map clearly shows the SEI layer's insulating behavior, with SEI-covered areas having lower conductivity compared to the pristine, conductive regions. Figures 3c–e show zoomed views, representing the morphology of the SEI microspot, the current image (c-AFM) and the phase map. Despite the larger size of the microspot formed in the ether-based electrolyte, the SEI structure still consisted of two distinct sub-layers. The first layer was again a thin, uniform layer approximately 10–14 nm thick (Figure 3f), which is in agreement with findings reported by

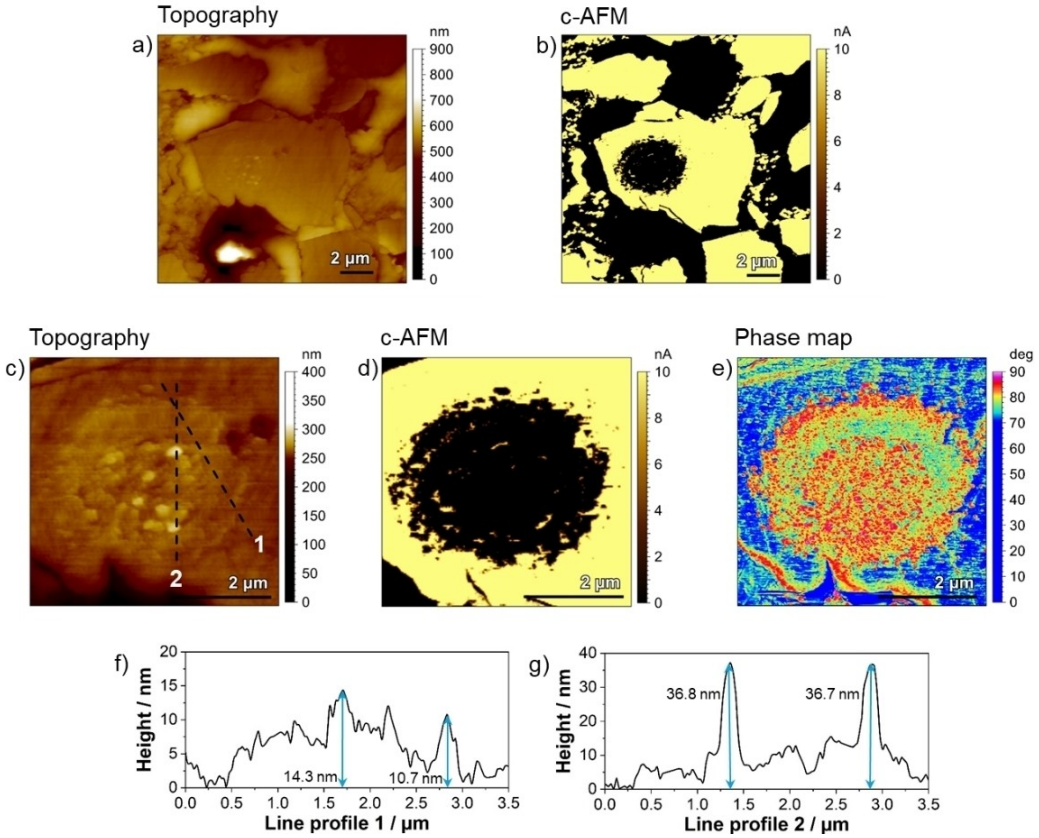

Figure 3. Characterization of the HC particle after SEI formation using SECCM with 1 charge-discharge cycle in 1 M $NaPF_6$ in diglyme. (a) Topography and (b) c-AFM image of the HC particle with the localized SEI deposition. (c) Zoomed topography image, revealing the morphology of the SEI layer. (d) Zoomed view c-AFM image of the topography image shown in (c), revealing the conductive area of the pristine HC surface and the insulating nature of the SEI layer. (e) Phase map illustrating variations in the phase contrast across the SEI layer. Line profiles (f) and (g) taken at indicated dashed lines in (c) showing the surface height variations.

Dong et al.,[61] who observed a thin SEI film with a high inorganic content in ether-based electrolytes, determined by ex-situ using cryo-TEM and XPS depth profiling. This thin layer is again covered by a heterogeneous layer of particulate deposits, with an average thickness of 36.3 ± 7 nm ($n = 5$, same particle, different areas) (Figure 3g).

To further investigate the SEI microspots, we also performed phase mapping (Figure 3e) in non-contact mode at the same spot. Phase imaging, which measures the phase lag between the driving signal of the oscillating AFM probe and the probe's response, as it interacts with different regions of the sample surface, gives qualitative insights into the nanomechanical properties of the sample. The phase map shows a higher phase lag for the particulate deposits, which points towards that they have different mechanical or viscoelastic properties compared to the thinner underlying SEI layer. Taking the phase image into account (Figure 3e), we assume that the layer-by-layer SEI structure on HC, with an inorganic-rich inner layer and a "softer", organic-rich outer layer is obtained, which was also reported by Pan et al.[62] They assumed that the effectiveness of the SEI formed on HC electrodes is not only dependent on its chemical composition but rather on the distribution of the compounds within the layers.

The phase map also supports the layer-by-layer model rather than the mosaic model of the SEI structure, which suggests a heterogeneous distribution of different SEI components "side-by-side" within the same layer. For the mosaic structure, we would expect to observe varying phase lags even among closely positioned deposits. However, significant phase differences appear only between the distinct SEI layers. This uniformity in phase lag among the deposits within the same layer strengthen the concept of a layered SEI structure model, where material properties change only between well-defined layers rather than within the same layer. This aligns with the findings of Lu and coworkers,[63] who reported different mechanical properties within SEI sub-layers for graphite electrodes in ether- and carbonate-based electrolytes. They reported that an ether-derived SEI forms an organic outer layer, which allows it to adapt to the volume expansion of graphite during cycling, while the distribution of inorganic compounds in the inner layer improves the Young's modulus, providing higher mechanical stability of the SEI. We also conducted AFM force spectroscopy measurements on the SEI formed in $NaPF_6$ in digylme as shown in Figure S4. Three different areas were probed, a HC area outside the SECCM deposited SEI microspot, the thin layer area of the SEI spot and the observed particulate deposits on the thin layer. The adhesion force and the Young's

modulus was determined for these three areas. It was found that the thin layer part of the SEI layer is on average less adhesive than the pristine HC particles (19.2 ± 6.2 nN vs 8.3 ± 5.7 nN, reflecting 57 % less adhesion; n = 100), which we assume is inorganic in nature. Due to hydrophilic-hydrophobic interactions between the clean silicon AFM tip, which is hydrophilic in nature and the inorganic compounds of the SEI layer most likely species like NaF, the adhesion force is low. The deposits of the upper SEI layer exhibit adhesion properties similar to those of the pristine particles (21.9 ± 6.2 nN; n = 100). This higher adhesion force is in agreement with the hydrophilic-hydrophilic interaction of organic compounds formed in the presence of FEC in the electrolyte. The reduced adhesion of the SEI layer is also clearly illustrated in the adhesion map and is in agreement with a previous study from our group,[43] although it should be noted that a different electrolyte and cycling parameters were used. The Young's Modulus values for the probed areas showed rather small changes in variation (pristine: 1.41 ± 0.42 GPa; thin SEI layer: 0.82 ± 0.70 GPa; particulate deposits: 1.71 ± 0.52 GPa; n = 100). The observed high variation of the data may result from probing the underlying HC in thin film areas, leading to potentially inaccurate values. Overall, the Young's modulus is similar to previous studies of our group for SEI formation on HC in $NaClO_4$ in PC.[43]

To further characterize the SEI microspots on the HC particles, we performed Raman measurements. Figure S5 shows extracted Raman spectra from a line-scan across a HC particle and SEI microspot. Two distinct bands at 1312 cm^{-1} (D), associated with defect-induced vibrations and at 1590 cm^{-1} (G) corresponding to the E2g graphitic mode are observed.[64] The graphitization degree can be evaluated using the intensity ratio of the D band to the G band. A higher I_D/I_G ratio indicates an increased presence of defects or structural disorder. The pristine HC particle shows a higher ratio ($I_D/I_G = 1.26$) compared with the SEI deposit ($I_D/I_G = 0.97$), reflecting an increased structural disorder and defect density. Notably, apart from the I_D/I_G ratio, which is also in agreement with our previous study,[18] no additional peaks were observed in the spectrum that could be attributed to the SEI spot. This may be associated with spot size and that only 1 cycle was performed.

Energy-dispersive X-ray spectroscopy (EDX) analyses were performed to compare pristine HC particles with the cycled ones. The emergence of a new peak in the EDX spectrum of the SECCM spot, which can be attributed to the presence of sodium, clearly indicates sodium being involved in the formation of the SEI layer during electrochemical cycling (Figure S6.) The EDX map reveals a significantly higher concentration of sodium across the entire area of the cycled spot in comparison to pristine HC.

To study the chemical composition of the locally formed deposits on the HC particles, we performed ToF-SIMS. For an introduction to this mass spectrometric imaging method and its applications in battery research, the interested reader is referred to a publication by Lombardo et al.[65] By combination of the 3D mass spectrometric data sets with AFM topography scans, we were able to get topography corrected spatially resolved 3D mass maps. SECCM generated SEI spots obtained with $NaPF_6$/diglyme using the same experimental conditions as for the spot shown in Figure 3 were imaged with AFM-SIMS. Figure 4a shows the AFM topography scan. A white arrow points to the

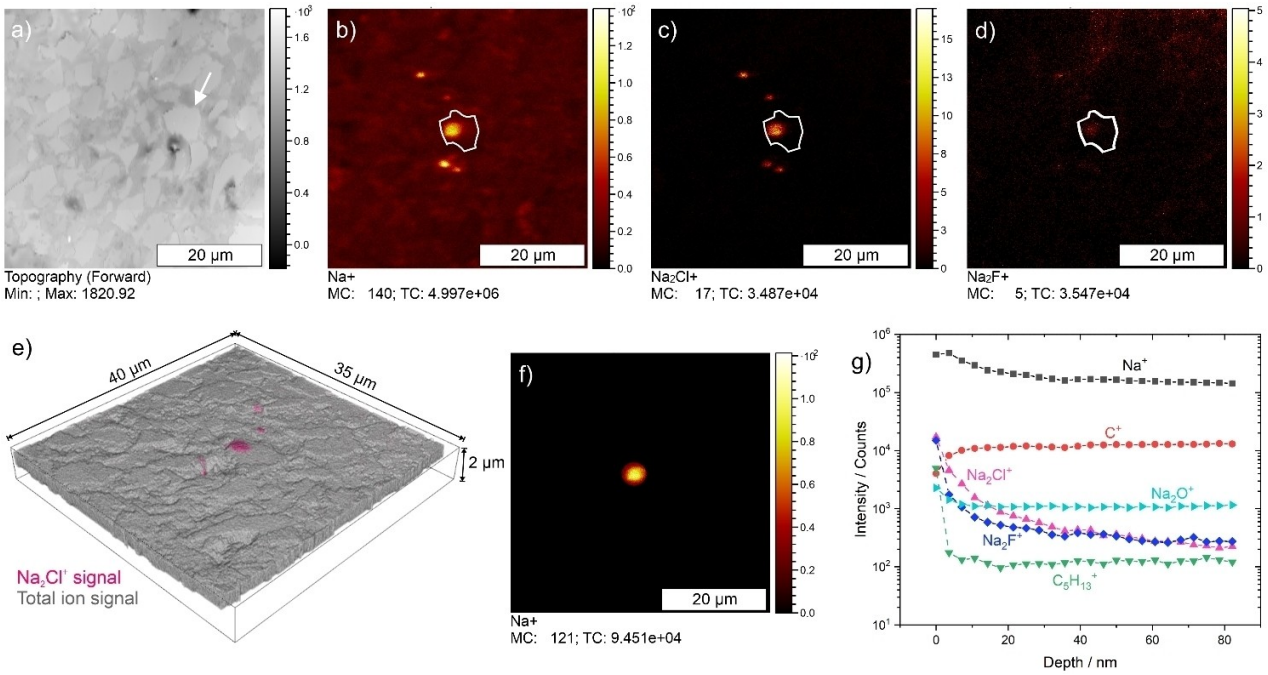

Figure 4. Correlative AFM-SIMS analysis of the particle that has been cycled in 1 M $NaPF_6$ in diglyme using SECCM. a) AFM topography scan before mass spectrometric analysis. The white arrow points to the HC particle of interest. (b, c, d) Cation images of selected mass fragments before depth profiling. e) Topography corrected 3D overlay mass image of Na_2Cl^- mass signal in pink and total ion signal in grey. f) Na^+ mass signal of the selected circular region of interest for the depth profile shown in g). g) Depth profile of the surface area that was in contact with the electrolyte in the SECCM experiment.

HC particle with the SEI microspot. Figures 4b-d show cation mass images of selected mass signals. The HC particle margins are traced with white lines. The chemical composition of the SEI microspot shows deposits of NaF, NaCl and Na_2O. This can be deduced from the depicted mass images (conf. Figures 4b-d) as well as the depth profile shown in Figure 4g. Interestingly, no mass signals characteristic for $NaCO_3$ or PF_6 appear in the region of the cycled HC particle. These were found in integral mass spectrometric data of a previous study of HC composite anodes that were cycled in the same electrolyte.[18] All of the mass signals that are related to the SEI are almost exclusively in the region of the electrode spot. The depth profile in Figure 4g shows that the Na_2Cl^+, Na_2F^+ and Na_2O^+ signals decline significantly within the first 20 nm and keep than constant. Obviously, small amounts of these compounds or of these secondary ions forming precursors are also within the HC. The chlorine in the NaCl is an impurity originating from the solvent that accumulates in the formed SEI, as already reported.[18] The high $C_5H_{13}^+$ count rate at the surface hints towards an outer organic layer, which is in good agreement with the phase map shown in Figure 3e. However, it cannot be excluded that adsorbed hydrocarbon compounds from the glovebox atmosphere also contribute to these mass fragments. Figure S7 and Figure S8 reveal single point measurements of a cycled spot in 1 M $NaPF_6$ in diglyme in negative and positive ion mode. In a previous work with the same HC and same electrolyte, we found a different composition of the SEI.[18] When examining the entire electrode, there are apparently deposits in the binder areas and we also measure its composition. These are then incorrectly assigned to the SEI. This highlights the importance of measuring SEI on individual, clean particles.

Investigating the Influence of the Scan Rate (1 Cycle)

Figure 5 shows AFM and c-AFM images revealing the effect of different scan rates on the morphology and blocking behaviour of the SEI spots formed via SECCM applying one charge-discharge cycle in 1 M $NaPF_6$ in diglyme as electrolyte. For a scan rate of 10 mV/s (Figure 5a), the topography shows a uniform and smooth SEI layer, indicating uniform deposition with a few higher deposits (Figure 5g), which overall causes a stable protection layer of the HC in the confined area of the SEI spot as clearly visible in the c-AFM image with a drop of the current of 100% (Figure 5d). In contrast, higher scan rates of 100 mV/s and 1000 mV/s (Figures 5b, c, e, f) result in more irregular and heterogeneous morphologies of the deposited SEI and quite heterogenous SEI coverage with a drop of the current to 72% and 76% for the scan rates of 100 mV/s and 1000 mV/s, respectively (Figures 5e and f). For these higher scan rates, the c-AFM images of the SEI layers show also heterogeneity in the blockage of the underlying conductive HC, likely corresponding to incomplete coverage of the HC surface by the formed SEI layer. Higher magnification images (Figures 5g–i) confirm this heterogeneity of the SEI layer at higher scan rates, with localized regions lacking proper SEI coverage.

The inhomogeneous formation of the SEI layer on HC composite anodes in diglyme-based electrolytes has been a topic of debate in the literature.[33,34,66] We hypothesize that the increased SEI inhomogeneities observed in diglyme are primarily due to the higher wettability of HC in diglyme compared to, for example, the carbonate-based EC/PC electrolyte. The contact angle measurements shown in Figure S3, clearly evidence that the average contact angle in diglyme is significantly smaller compared to EC/PC, leading to a larger and uneven spreading of the droplet in diglyme, resulting in inhomogeneous SEI deposition. In addition, the rapid ion and electron transfer at higher scan rates (e.g., 100 and 1000 mV/s in Figures 5e and f) can further disrupt SEI layer growth, resulting in even more heterogeneous structural features. We assume that the observed inhomogeneities are not related to solvent evaporation, as the low vapor pressure of diglyme compared to conventional organic solvents such as acetone suggests that its evaporation is negligible (e.g., acetone (~231 mmHg or 30.8 kPa), diglyme (~0.45 mmHg or 0.06 kPa), ethylene carbonate (~0.01 mmHg or 0.001 kPa) and propylene carbonate (~0.13 mmHg or 0.017 kPa).

Investigating the Effect of Cycling Number (Scan Rate: 10 mV/s)

Figure 6 shows the topography and c-AFM analysis of the SEI layer formed at different cycling numbers in 1 M $NaPF_6$ in diglyme applying 1, 10, and 40 charge-discharge cycles, respectively with a scan rate of 10 mV/s. For increasing cycling number, an insulating SEI is formed. However, compared to the localized SEI formation in EC/PC (see Figures 2a and b), the meniscus contact droplet formed with $NaPF_6$ in diglyme seems to spread for higher cycling numbers and the formed SEI is spread over a larger area (Figures 6b and e) for 10 cycles or covering almost the whole HC particle as clearly visible in Figures 6c and f. Interestingly, for 40 cycles, the HC particle in the topography image does not appear to be fully covered by the SEI as the upper part of the particle does not reveal any structure of SEI as typically observed in the topography images and shows polishing artefacts (lines), whereas the c-AFM clearly indicates that the whole HC particle is covered with an insulating layer. This data also confirms that the SEI remains stable, forming a uniform insulating layer under the given experimental conditions for repeated cycles, which is in agreement with studies reported by Pan et al.,[62] who showed stability of the SEI layer over 150 cycles in ether-based electrolyte for HC anodes for fast Na^+ ion storage and long-term cycling stability. It should be noted that the height profiles in Figures 6j–l do not show a clear correlation with the number of cycles, as the thickness of the deposition is not significantly increased over 40 cycles. While the formed SEI depositions are becoming more widespread, their growth in height remains limited. This suggests that the initial decomposition of the ether-based electrolyte forms a thin insulating layer, which prevents further electrolyte decomposition. The thin layers observed are in agreement with previous studies showing that

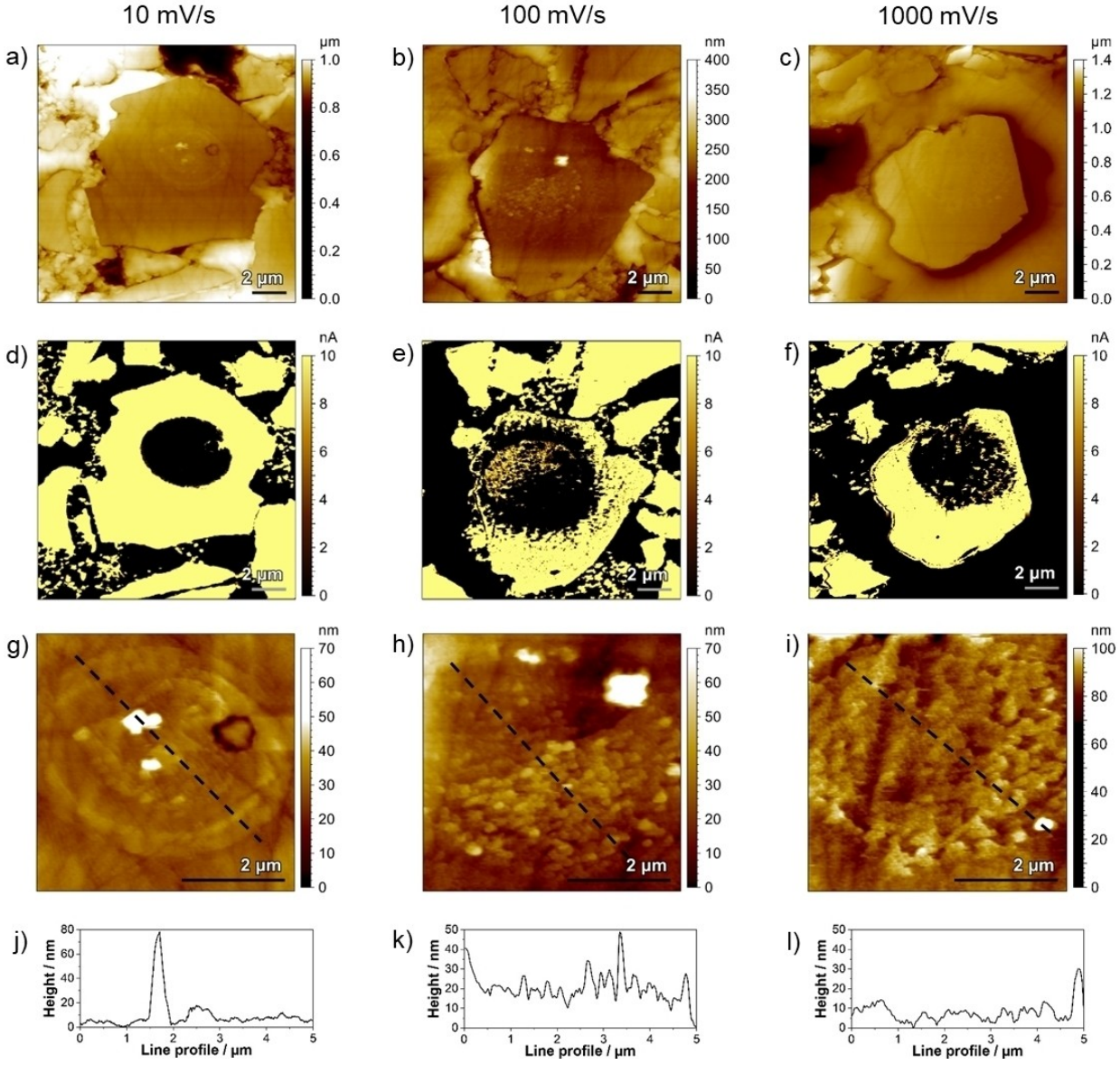

Figure 5. Topography (a, b, c) and c-AFM images (d, e, f) of different HC particles, showing confined SEI depositions using different electrochemical scan rates for one charge-discharge cycle. (g, h, i) present zoomed-in topographic images corresponding to (a, b, c), respectively. Line profiles (j, k, l) along the dashed lines in (g, h, i) illustrate surface height variations.

ether-based electrolytes form thinner SEI layers, which enhance charge transfer kinetics.[61,66]

To evaluate the influence of the electrolyte and to compare the influence on the SEI layer formation, SECCM experiments were performed using the same experimental conditions (scan rate and cycling number) in 1 M $NaPF_6$ in EC/PC (1 : 1) + 5 wt% FEC, as shown in Figures S9 and S10, respectively. As mentioned above, the wettability is much higher in diglyme (see contact angle measurements in Figure S3), which leads to a significant spreading of the droplet at longer cycling times that is observed to a much lesser extend in the experiments performed in 1 M $NaPF_6$ in EC/PC + 5% FEC. The diameter of the formed spot increased from 3.7 µm (1 cycle) to 5.1 µm (10 cycles) and 7.2 µm (40 cycles) as shown in Figure S10. In addition, the SEI layer obtained from the carbonate-based electrolyte (Figure S9) showed a uniform SEI with complete passivation at higher scan rates (100 and 1000 mV/s) in the first cycle, as shown by c-AFM measurement by a current drop of 100%. In contrast, SECCM experiments using diglyme resulted in irregular SEI morphologies (Figures 5b, c, e, f) with incomplete coverage and a reduction in current to 72% and 76% at 100 and 1000 mV/s, respectively. Longer cycling (up to 40 cycles) also resulted in differences based on the different electrolytes, which is in agreement with the findings of Dong et al.[61] In our study, the SEI layer obtained in 1 M $NaPF_6$ in diglyme increased from 10–14 nm in the first cycle to about 40 nm (10th cycle) and then remained relatively stable up to the 40th cycle forming an insulating layer. Experiments performed in 1 M $NaPF_6$ in EC/PC + 5% FEC resulted in continuous growth of the layer (see Figure S10), increasing from 20 nm (first cycle) to

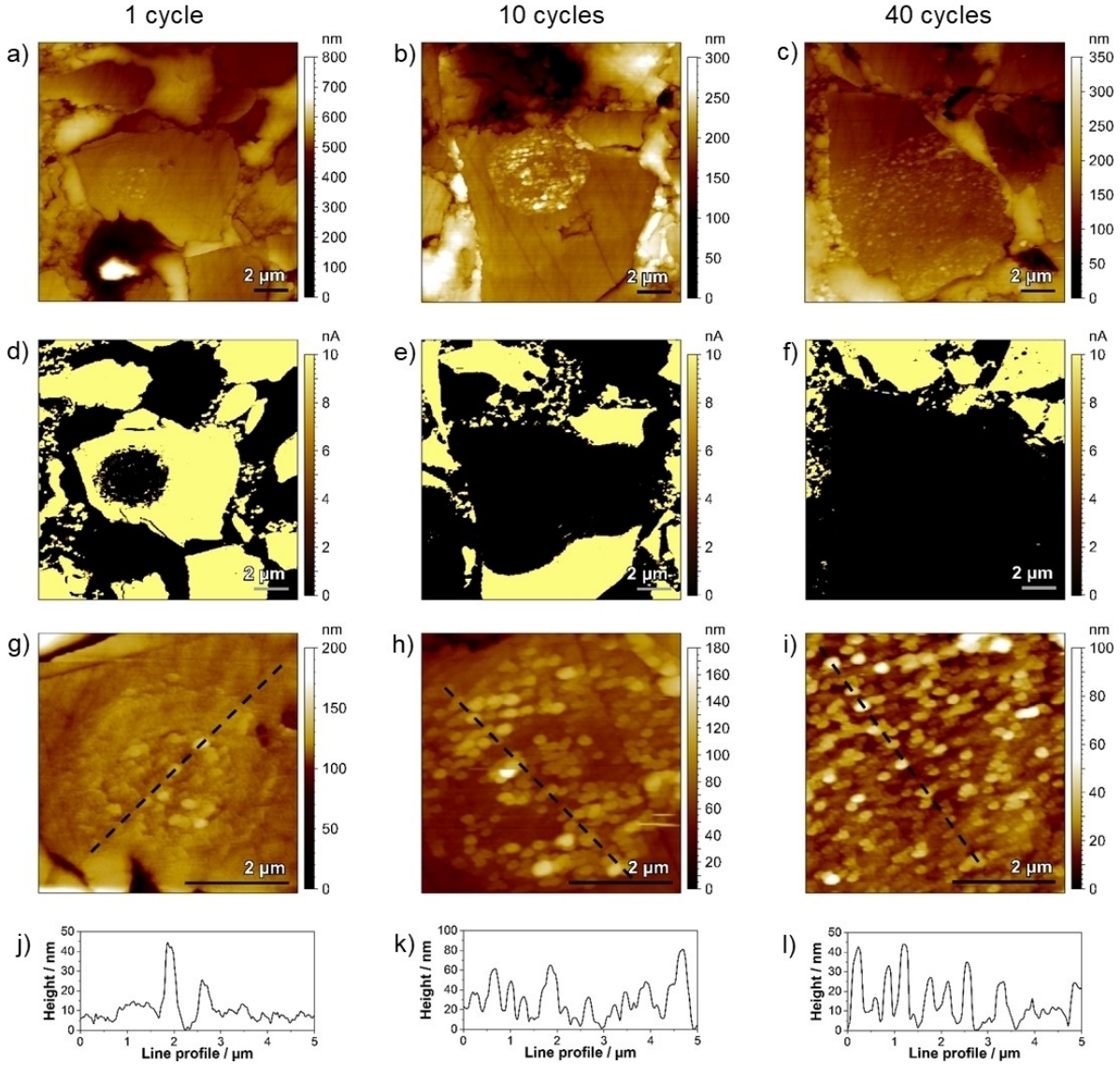

Figure 6. Topography (a, b, c) and c-AFM images (d, e, f) of different HC particles, showing SEI depositions after 1, 10, and 40 cycles, respectively, at a scan rate of 10 mV/s. (g, h, i) Zoomed-topographic images corresponding to (a, b, c), respectively. Line profiles (j, k, l) along the dashed lines in (g, h, i) illustrate surface height variation.

almost 1 µm in the 40th cycle. The observed differences may be related to the reported co-intercalation of solvated Na^+ in ether-based electrolytes[61] and the presence of the additive in the EC/PC. In the diglyme-based electrolyte, the composition of the SEI contains mainly sodium alkoxides rather than NaF, which is the dominant species in carbonate-based electrolytes with FEC. Overall, these results highlight distinct electrolyte-dependent changes in SEI formation. These observations are consistent with the study by Dong et al.,[61] where the relatively stable and thinner SEI in the ether-based electrolyte indicates a more controlled interphase formation, while the increasing SEI thickness in the carbonate-based electrolyte indicates continuous changes at the electrode interface. This difference may be related to the proposed solvated Na^+ co-intercalation mechanism in ether-based electrolytes,[61] as well as differences in electrolyte decomposition and SEI formation.

Figures S13 and S14 show exemplary cycling curves of the SECCM experiments using different experimental conditions. Compared to cycling the HC composite anodes in Swagelok cells, in half-cell configurations in ether- or carbonate-based electrolytes, the absence of a deinsertion peak during the oxidation process suggests that the inserted sodium is not fully released under the given experimental conditions. This could be due to partial sodium insertion during the reduction sweep, where de-intercalation of small amounts of inserted sodium may be difficult and require a higher driving force for extraction. Several studies have been performed on Li-ion batteries using SECCM, where the delithiation process is only partially observable or absent.[67,68] For example, Martin-Yerga et al. observed that, in contrast to macroscale experiments, only one delithiation process was observed and delithiation became

visible only when the SECCM test was performed with larger micropipettes (~30 μm in diameter).[59]

Conclusions

A uniform SEI layer on the negative electrode of SIBs is the key factor influencing the overall battery performance. Despite the number of recent studies, the SEI formation is still not fully understood and data for different electrolytes yield varying results. Here, we used SECCM for the localized formation of SEI microspots deposited on embedded and polished, single HC particles, which allowed us to characterize the height and morphology of the formed SEI layer. Our measurements indicate that the SEI layer consists of two layers: a thin, smooth, and uniform layer adjacent to the HC surface, and a thicker, more heterogeneous layer with individual particulate deposits on top of this thin SEI layer. c-AFM, force spectroscopy and AFM-ToF-SIMS allowed us to further characterize the SEI microspots with respect to the electronic insulating nature, e.g., as a function of the different cycling number and scan rates, the nanomechanical properties, and the chemical composition. Our results contribute to information on the structure of the SEI formed in different electrolyte compositions but also support the layer-by-layer model of the SEI. Using SECCM opens up the possibility to study the SEI formation on different electrode anode and cathode materials in various electrolytes allowing for screening experiments using the same electrode. It should be noted, however, that such studies require samples that are relatively flat.

Experimental Section

Materials

HC active material (Kuranode, 5 μm, Type II) was sourced from Kuraray, Japan. Sodium carboxymethyl cellulose (Na-CMC), 1-methoxy-2-(2-methoxyethoxy)ethane (diglyme), and sodium hexafluorophosphate ($NaPF_6$), were obtained from Sigma-Aldrich, Germany. Sodium metal was purchased from Alfa Aesar, Germany, and carbon black (Super P) was sourced from Thermo Scientific, USA.

For the presented studies, two different electrolytes were used. The primary reference electrolyte was 1 M $NaPF_6$ in EC/PC (1 : 1 wt%) + 5 wt% FEC with a water content determined to be below 20 ppm using Karl-Fischer titration. This electrolyte is used as reference electrolyte for Round Robin tests within the POLiS Cluster of Excellence. Electrolyte preparation was done by mixing the solvents in aluminum containers, followed by transferring to aluminum vials, which were sealed inside a glovebox. Each vial remained sealed until used inside the glove box, ensuring minimal exposure. Further details can be found in the publication by Smith et al.[69] Additionally, 1 M $NaPF_6$ in diglyme was prepared again within the glovebox. The water content was below 10 ppm as determined by Karl-Fischer titration.

Electrodes

The electrodes used in this study were composed of 85 wt.% hard carbon (Kuranode type II, 5 μm), 10 wt.% Super P, and 5 wt.% Na-CMC binder, coated (doctor-bladed) on an aluminum current collector. To achieve a flat surface and minimizing artifacts for SECCM and AFM measurements, the electrodes were embedded in EpoFix (Struers GmbH, Germany) resin, allowing the cross section of the electrode to be polished (see Figure S11) following a procedure described elsewhere.[43] To ensure electrical conductivity for electrochemical and c-AFM measurements, the backside of each sample was attached to a stainless-steel support using silver adhesive. Figure S11 shows an optical microscopic image of the embedded and polished sample.

Prior to each experiment, sodium was freshly electroplated at $E = -0.2$ V vs Na/Na^+ in 1 M $NaPF_6$ in EC/PC onto a copper wire to obtain a reference electrode that fits into the SECCM pipette. The stability of the Na-electroplated wire was evaluated by measuring the open circuit potential (OCP) against sodium. Stability of the potential was observed for 5 days after plating, with an OCP value of approximately ~0.0 V, indicating that the reference electrode is sufficiently stable (see Figure S12).

Scanning Electrochemical Cell Microscopy

Electrochemical experiments were performed using SECCM, as schematically illustrated in Figure 1a. The scanning ion conductance (SICM) and SECCM scan head of the Park NX10 (Park Systems, South Korea) housed within an Ar-filled glovebox (Unilab, MBraun, $O_2 <$ 0.1 ppm, $H_2O <$ 0.1 ppm) was used to conduct SECCM experiments. Borosilicate pipettes with a tip inner diameter of approximately 1 μm (Figure S1), were obtained from Park Systems. The pipettes were filled with an electrolyte solution using a MicroFil tip (MicroFil 67, WPI Instruments, Germany), and subsequently, the Na reference electrode was inserted. To approach the electrode surface, the pipette was approached at a rate of 0.1 μm/s using the z-piezo of the SICM scan head. The ion current was monitored, and a sharp change in current indicated the formation of an electrochemical liquid cell as the probe's liquid meniscus contacts the surface of the selected HC particle. CV was performed using a bipotentiostat (CHI760E, CH Instruments, USA) combined with a preamplifier (CHI200B Picoamp Booster, CH Instruments) in a two-electrode setup with the embedded HC as working and the Na reference electrode as counter/reference electrode at different scan rates in the potential range of 0.001–2.0 V vs Na/Na^+. The faradaic current output signal from the bipotentiostat was routed to the AFM controller through an analog-to-digital conversion channel and displayed by the scan software (SmartScan, Park Systems). The SECCM measurements were repeated under identical conditions, mainly on the central regions of the HC particles. A major advantage of this approach is that we were able to perform multiple experiments on the same sample, where different HC particles have quite similar and uniform roughness parameters as all HC particles were located on one single polished sample, ensuring consistent surface preparation and roughness across the electrode (see Figure S15).

SPM Measurements

Atomic Force Microscopy Measurements

After the SEI microspots were formed using SECCM, the samples were carefully rinsed with dimethyl carbonate (DMC), three times in the same electrochemical cell. DMC is commonly used for rinsing, as it has been reported in the literature that the surface composition of the SEI layer on HC is not significantly altered.[70]

The AFM head of the Park NX10 was used to conduct AFM experiments of the dried samples. c-AFM measurements were

performed using sharp, conductive, single-crystal diamond probes (AD-2.8-AS, Oxford Instruments, UK) with a nominal spring constant of 2.8 N/m and a resonant frequency of 65 kHz and conductive diamond coated probes (All-In-One-DD, BudgetSensors, USA) with a nominal spring constant of 6.5 N/m and a resonant frequency of 110 kHz. The scan speed was set to 0.3 Hz, with an applied potential of 1 V between the sample and the tip.

Low-force contact mode imaging ($F = 5$ nN), force spectroscopy, and nanomechanical mapping were performed using etched silicon probes (RTESPAW-150, Bruker, Germany) with a nominal spring constant of 6.0 N/m and a nominal resonance frequency of 150 kHz. Before measurements, the force constants of the cantilevers were determined using the thermal noise method.[71] Force-distance curves were recorded at a sweep rate of 1 μm/s with loading forces of 10 nN. The nanomechanical mappings (30.0×30.0 μm^2, 512×512 pixels) were recorded in PinPoint mode utilizing loading force of 10 nN at a sweep rate of 5 μm/s [1]. Phase mapping was recorded in non-contact mode (NCM) using a doped silicon probe (AC160TS-R3, Oxford Instruments, UK) with a nominal spring constant of 26 N/m and a resonance frequency of 300 kHz. AFM images and force-distance curves were evaluated using Mountain SPIP software (version 9.1.9908, Digital Surf, France). The topography images were levelled to eliminate any surface tilt. We applied noise correction to remove unwanted artifacts, such as noise lines in the maps where necessary. The raw data are avaialble from Zenodo (DOI: 10.5281/zenodo.14445595, reference number 439). The raw data were used to generate the CV plots (Origin software was used for plotting).

SEM/EDX and Raman Spectroscopy

SEM imaging and EDX were performed with Quanta 3D FEG and Apreo 2 s (Thermo Fisher Scientific, Netherlands). SEM images were obtained at 5 kV, 50 pA and EDX measurements using a primary electron beam at 5 kV, 4 nA. EDX mappings were performed using EDAX Element EDS detector (EDAX, Germany) with a resolution of 512×400 pixels, 32 frames and a dwell time of 50 μs. Raman spectra of the HC samples with the SEI microspots were recorded over a spectral range from 100 to 3700 cm^{-1} (alpha300 R, WITec GmbH, Germany) with an excitation wavelength of 532 nm, 200 micro-Watt laser power for 3 s (5 repetitions) and Uhts-300 detector, 1800 n/mm grid and a 50× objective (NA = 0.7). Data was processed using Origin (OriginPro 2019b, OriginLab, USA).

AFM-ToF-SIMS

Correlative AFM-SIMS analysis was carried out with a M6 Plus ToF-SIMS instrument (IONToF GmbH, Münster, Germany). The instrument is equipped with a Bi50 nanoprobe analysis gun and a 2 keV EI source for sputtering. Samples can be reproducibly moved back and forth between SIMS and the scanning probe module (SPM) measuring positions by a piezoelectrically driven stage. The SPM scanner can analyze an area of up to 80×80×10 μm^3. SIMS imaging was carried out with 60 keV Bi_3^{2+} primary ions by operating the source in fast imaging mode ($I = 0.116$–0.119 pA @ cycle time 100 μs, beam defining aperture 200 μm). The ToF-analyser was operated in delayed extraction mode (extraction delay = -0.010 μs). In order to enhance transmission, the topography mode was applied. For charge compensation, the low energy electron flood gun was used and in addition the main chamber flooded with Ar ($p = 5 \cdot 10^{-6}$ mbar). The obtained mass resolution (FWHM) was better than 1,100 @ m/z 23.0 (Na^+) in positive and better than 1,000 @ m/z 35.0 (Cl^-) in negative ion mode. For surface imaging of single particles, the analysis beam was scanned in random mode and 512×512 pixels were measured on an area of 50×50 μm^2. The dose density was kept below 10^{13} ions/cm^2 to maintain static conditions.

A 1 keV Ar^+ beam ($I = 306.9$ nA) was used for depth profiling in non-interlaced mode with a pause time for charge compensation of 4 s. Analysis was carried out on an area of 40×40 μm^2 centered to a sputter removal area of 250×250 μm^2. Before depth profiling, the topography of the sample surface (50×50 μm^2, 128×2048 pixels) was scanned in tapping® mode with the SPM. For depth profiling 15 analysis frames were measured per image layer alternating with 1 sputter frame. Finally, a further topography scan was recorded with the SPM. The whole data evaluation including correlation of AFM and mass spectrometric data was carried out with the SurfaceLab 7.4 software (IONToF GmbH).

Supporting Information

Supplementary material associated with this article can be found, in the online version, at DOI 10.5281/zenodo.14445595, reference 439.

Acknowledgements

The Focused Ion Beam Center UUlm (IABC) is acknowledged. Simon Schauer and Mika Lindén (Institute of Inorganic Chemistry II, Ulm University) are thanked for the Raman measurements. Andreas Hofmann and Anna Smith (Karlsruhe Institute of Technology (KIT)) are acknowledged for providing the EC/PC reference electrolyte. This work contributes to the research performed at CELEST (Center for Electrochemical Energy Storage Ulm – Karlsruhe) and was funded by the Deutsche Forschungsgemeinschaft (DFG, German Research Foundation) under Germany's Excellence Strategy – EXC 2154 – Project number 390874152 (POLiS Cluster of Excellence). MR and DS thank the BMBF for funding the AFM-SIMS within the ProGrAL project (FKZ 03XP0427). Open Access funding enabled and organized by Projekt DEAL.

Conflict of Interests

The authors declare no conflict of interest.

Data Availability Statement

The data that support the findings of this study are openly available in Zenodo DOI: 10.5281/zenodo.14445595, reference number 439.

Keywords: Localized solid electrolyte interphase (SEI) · scanning electrochemical cell microscopy (SECCM) · hard carbon composite anode · atomic force microscopy (AFM) · secondary ion mass spectrometry (SIMS)

[1] E. Peled, *J. Electrochem. Soc.* **1979**, *126*, 2047–2051.

[2] E. Peled, D. Golodnitsky, G. Ardel, *J. Electrochem. Soc.* **1997**, *144*, L208.
[3] D. Aurbach, Y. Ein-Ely, A. Zaban, *J. Electrochem. Soc.* **1994**, *141*, L1–L3.
[4] K. Kanamura, H. Tamura, S. Shiraishi, Z. Takehara, *J. Electrochem. Soc.* **1995**, *142*, 340.
[5] K. Xu, *Chem. Rev.* **2004**, *104*, 4303–4417.
[6] R. L. Sacci, J. M. Black, N. Balke, N. J. Dudney, K. L. More, R. R. Unocic, *Nano Lett.* **2015**, *15*, 2011–2018.
[7] Y. Gu, E. M. You, J. De Lin, J. H. Wang, S. H. Luo, R. Y. Zhou, C. J. Zhang, J. L. Yao, H. Y. Li, G. Li, W. W. Wang, Y. Qiao, J. W. Yan, D. Y. Wu, G. K. Liu, L. Zhang, J. F. Li, R. Xu, Z. Q. Tian, Y. Cui, B. W. Mao, *Nat. Commun.* **2023**, *14*, 1082 .
[8] W. W. Wang, Y. Gu, H. Yan, K. X. Li, Z. Bin Chen, Q. H. Wu, C. Kranz, J. W. Yan, B. W. Mao, *Faraday Discuss.* **2021**, *233*, 190–205.
[9] J. Zhang, J. Gai, K. Song, W. Chen, *Cell Rep. Phys. Sci.* **2022**, *3*, 100868.
[10] S. J. An, J. Li, C. Daniel, D. Mohanty, S. Nagpure, D. L. Wood, *Carbon* **2016**, *105*, 52–76.
[11] M. D. Bouguern, A. K. MR, K. Zaghib, *J. Power Sources* **2024**, *623*, 235457.
[12] W. Guo, Y. Meng, Y. Hu, X. Wu, Z. Ju, Q. Zhuang, *Front Energy Res.* **2020**, *8*, 170.
[13] M. Á. Muñoz-Márquez, D. Saurel, J. L. Gómez-Cámer, M. Casas-Cabanas, E. Castillo-Martínez, T. Rojo, *Adv. Energy Mater.* **2017**, *7*, 1700463.
[14] M. Hou, Y. Zhou, F. Liang, H. Zhao, D. Ji, D. Zhang, L. Li, Y. Lei, *J. Chem. Eng.* **2023**, 146227.
[15] A. Ponrouch, E. Marchante, M. Courty, J.-M. Tarascon, M. R. Palacín, *Energy Environ. Sci.* **2012**, *5*, 8572.
[16] Y. Li, L. Mu, Y. S. Hu, H. Li, L. Chen, X. Huang, *Energy Storage Mater.* **2016**, *2*, 139–145.
[17] Q. Meng, Y. Lu, F. Ding, Q. Zhang, L. Chen, Y. S. Hu, *ACS Energy Lett.* **2019**, *4*, 2608–2612.
[18] K. Palanisamy, S. Daboss, J. Romer, D. Schäfer, M. Rohnke, J. K. Flowers, S. Fuchs, H. S. Stein, M. Fichtner, C. Kranz, *Batter. Supercaps* **2024**, *7*, e202300482.
[19] P. Bai, Y. He, P. Xiong, X. Zhao, K. Xu, Y. Xu, *Energy Storage Mater.* **2018**, *13*, 274–282.
[20] C. Wu, Y. Yang, Y. Zhang, H. Xu, X. He, X. Wu, S. Chou, *Chem. Sci.* **2024**, *15*, 6244–6268.
[21] B. Xiao, T. Rojo, X. Li, *ChemSusChem.* **2019**, *12*, 133–144.
[22] Y. Kim, K. Ha, S. M. Oh, K. T. Lee, *Chem. Eur. J.* **2014**, *20*, 11980–11992.
[23] S. Tan, H. Yang, Z. Zhang, X. Xu, Y. Xu, J. Zhou, X. Zhou, Z. Pan, X. Rao, Y. Gu, *Molecules* **2023**, *28*, 3134.
[24] D. A. Stevens, J. R. Dahn, *J. Electrochem. Soc.* **2001**, *148*, A803.
[25] C. Matei Ghimbeu, A. Beda, B. Réty, H. El Marouazi, A. Vizintin, B. Tratnik, L. Simonin, J. Michel, J. Abou-Rjeily, R. Dominko, *Adv. Energy Mater.* **2024**, *14*, 2303833.
[26] Y. Pan, Y. Zhang, B. S. Parimalam, C. C. Nguyen, G. Wang, B. L. Lucht, *J. Electroanal. Chem.* **2017**, *799*, 181–186.
[27] F. A. Soto, P. Yan, M. H. Engelhard, A. Marzouk, C. Wang, G. Xu, Z. Chen, K. Amine, J. Liu, V. L. Sprenkle, *Adv. Mater.* **2017**, *29*, 1606860.
[28] E. Peled, S. Menkin, *J. Electrochem. Soc.* **2017**, *164*, A1703.
[29] J. Lee, J. Kim, S. Kim, C. Jo, J. Lee, *Mater. Adv.* **2020**, *1*, 3143–3166.
[30] M. Sawicki, L. L. Shaw, *RSC Adv.* **2015**, *5*, 53129–53154.
[31] S. K. Heiskanen, J. Kim, B. L. Lucht, *Joule* **2019**, *3*, 2322–2333.
[32] Z. Yu, J. Song, D. Wang, D. Wang, *Nano Energy* **2017**, *40*, 550–558.
[33] K. Westman, R. Dugas, P. Jankowski, W. Wieczorek, G. Gachot, M. Morcrette, E. Irisarri, A. Ponrouch, M. R. Palacín, J.-M. Tarascon, P. Johansson, *ACS Appl. Energy Mater.* **2018**, *1*, 2671–2680.
[34] J. Pan, Y. Sun, Y. Yan, L. Feng, Y. Zhang, A. Lin, F. Huang, J. Yang, *JACS Au* **2021**, *1*, 1208–1216.
[35] H. Alptekin, H. Au, E. Olsson, J. Cottom, A. C. S. Jensen, T. F. Headen, Q. Cai, A. J. Drew, M. Crespo Ribadeneyra, M. Titirici, *Adv. Mater. Interfaces* **2022**, *9*, 2101267.
[36] I. V. Veryovkin, C. E. Tripa, A. V. Zinovev, S. V. Baryshev, Y. Li, D. P. Abraham, *Nucl. Instrum. Methods Phys. Res. B* **2014**, *332*, 368–372.
[37] K. Edström, T. Gustafsson, J. O. Thomas, *Electrochim. Acta* **2004**, *50*, 397–403.
[38] M. Golozar, A. Paolella, H. Demers, S. Bessette, M. Lagacé, P. Bouchard, A. Guerfi, R. Gauvin, K. Zaghib, *Commun. Chem.* **2019**, *2*, 131.
[39] L. Danis, S. M. Gateman, C. Kuss, S. B. Schougaard, J. Mauzeroll, *ChemElectroChem* **2017**, *4*, 6–19.
[40] H. Wu, H. Jia, C. Wang, J. G. Zhang, W. Xu, *Adv. Energy Mater.* **2021**, *11*, 2003092.
[41] Y. Chu, Y. Shen, F. Guo, X. Zhao, Q. Dong, Q. Zhang, W. Li, H. Chen, Z. Luo, L. Chen, *Electrochem. Energy Rev.* **2020**, *3*, 187–219.
[42] R. Kempaiah, G. Vasudevamurthy, A. Subramanian, *Nano Energy* **2019**, *65*, 103925.
[43] S. Daboss, T. Philipp, K. Palanisamy, J. Flowers, H. S. Stein, C. Kranz, *Electrochim. Acta* **2023**, *453*, 142345.
[44] Z. He, W. Li, Y. Chen, F. Huang, Y. Jie, X. Li, R. Cao, S. Jiao, *Batter. Energy* **2024**, *3*, 20230045.
[45] G. Zampardi, S. Klink, V. Kuznetsov, T. Erichsen, A. Maljusch, F. La Mantia, W. Schuhmann, E. Ventosa, *ChemElectroChem* **2015**, *2*, 1607–1611.
[46] S. D. Lacey, J. Wan, A. von W. Cresce, S. M. Russell, J. Dai, W. Bao, K. Xu, L. Hu, *Nano Lett.* **2015**, *15*, 1018–1024.
[47] J. Zhang, R. Wang, X. Yang, W. Lu, X. Wu, X. Wang, H. Li, L. Chen, *Nano Lett.* **2012**, *12*, 2153–2157.
[48] S. Ramdon, B. Bhushan, *J. Power Sources* **2014**, *246*, 219–224.
[49] N. Balke, S. Jesse, A. N. Morozovska, E. Eliseev, D. W. Chung, Y. Kim, L. Adamczyk, R. E. García, N. Dudney, S. V. Kalinin, *Nat. Nanotechnol.* **2010**, *5*, 749–754.
[50] M. Wang, Z. Song, J. Bi, H. Li, M. Xu, Y. Gong, Y. Zhou, Y. Zhao, K. Yang, *Batter. Energy* **2023**, *2*, 20230006.
[51] S.-Y. Lang, R. Wen, *Curr. Opin. Electrochem.* **2024**, *46*, 101523.
[52] S. Y. Luchkin, S. A. Lipovskikh, N. S. Katorova, A. A. Savina, A. M. Abakumov, K. J. Stevenson, *Sci. Rep.* **2020**, *10*, 8550.
[53] X.-R. Liu, X. Deng, R.-R. Liu, H.-J. Yan, Y.-G. Guo, D. Wang, L.-J. Wan, *ACS Appl. Mater. Interfaces* **2014**, *6*, 20317–20323.
[54] H.-J. Guo, H.-X. Wang, Y.-J. Guo, G.-X. Liu, J. Wan, Y.-X. Song, X.-A. Yang, F.-F. Jia, F.-Y. Wang, Y.-G. Guo, R. Wen, L.-J. Wan, *J. Am. Chem. Soc.* **2020**, *142*, 20752–20762.
[55] Z. Zhang, K. Smith, R. Jervis, P. R. Shearing, T. S. Miller, D. J. L. Brett, *ACS Appl Mater. Interfaces* **2020**, *12*, 35132–35141.
[56] A. Kumatani, Y. Takahashi, C. Miura, H. Ida, H. Inomata, H. Shiku, H. Munakata, K. Kanamura, T. Matsue, *Surf. Interface Anal.* **2019**, *51*, 27–30.
[57] S. Daboss, F. Rahmanian, H. S. Stein, C. Kranz, *Electrochem. Sci. Adv.* **2022**, *2*, e2100122.
[58] Y. Takahashi, T. Yamashita, D. Takamatsu, A. Kumatani, T. Fukuma, *Chem. Commun.* **2020**, *56*, 9324–9327.
[59] D. Martín-Yerga, M. Kang, P. R. Unwin, *ChemElectroChem* **2021**, *8*, 4240–4251.
[60] M. E. Lee, S. M. Lee, J. Choi, D. Jang, S. Lee, H. J. Jin, Y. S. Yun, *Small* **2020**, *16*, 2001053.
[61] R. Dong, L. Zheng, Y. Bai, Q. Ni, Y. Li, F. Wu, H. Ren, C. Wu, *Adv. Mater.* **2021**, *33*, 2008810.
[62] M. Ma, H. Cai, C. Xu, R. Huang, S. Wang, H. Pan, Y. Hu, *Adv. Funct. Mater.* **2021**, *31*, 2100278.
[63] Z. Wang, H. Yang, Y. Liu, Y. Bai, G. Chen, Y. Li, X. Wang, H. Xu, C. Wu, J. Lu, *Small* **2020**, *16*, 2003268.
[64] X. Dou, I. Hasa, D. Saurel, C. Vaalma, L. Wu, D. Buchholz, D. Bresser, S. Komaba, S. Passerini, *Mater. Today* **2019**, *23*, 87–104.
[65] T. Lombardo, F. Walther, C. Kern, Y. Moryson, T. Weintraut, A. Henss, M. Rohnke, *J. Vac. Sci. Technol.* **2023**, *41*, 053207.
[66] X. Yin, Z. Wang, Y. Liu, Z. Lu, H. Long, T. Liu, J. Zhang, Y. Zhao, *Nano Res.* **2023**, *16*, 10922–10930.
[67] D. Martín-Yerga, D. C. Milan, X. Xu, J. Fernández-Vidal, L. Whalley, A. J. Cowan, L. J. Hardwick, P. R. Unwin, *Angew. Chem. Int. Ed.* **2022**, *61*, e202207184.
[68] X. Xu, D. Martín-Yerga, N. E. Grant, G. West, S. L. Pain, M. Kang, M. Walker, J. D. Murphy, P. R. Unwin, *Small* **2023**, *19*, 2303442.
[69] P. Stüble, C. Müller, N. Bohn, M. Müller, A. Hofmann, T. Akçay, J. Klemens, A. Koeppe, S. Kolli, D. Rajagopal, H. Geßwein, W. Schabel, P. Scharfer, M. Selzer, J. R. Binder, A. Smith, *Batter. Supercaps* **2024**, *7*, e202400406.
[70] J. Fondard, E. Irisarri, C. Courrèges, M. R. Palacin, A. Ponrouch, R. Dedryvère, *J. Electrochem. Soc.* **2020**, *167*, 070526.
[71] J. L. Hutter, J. Bechhoefer, *Rev. Sci. Instrum.* **1993**, *64*, 1868–1873.

Manuscript received: December 23, 2024
Revised manuscript received: February 18, 2025
Version of record online: ■■, ■■

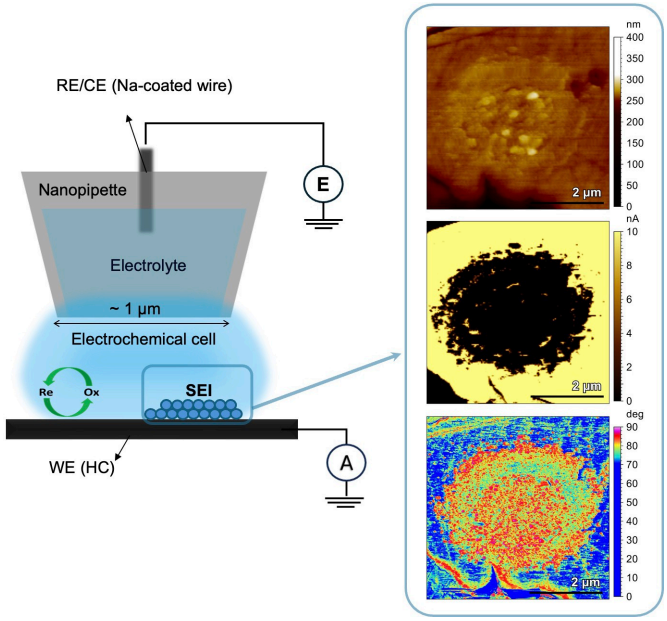

The local formation of the solid electrolyte interphase (SEI) on hard carbon is demonstrated by scanning electrochemical cell microscopy (SECCM). The formation of SEI microspots allows the direct study of the effects of the electrolyte composition and experimental parameters on the morphology, height, passivation and nanomechanical properties of the SEI using an SPM instrument, capable of switching the scan head from SECCM to AFM.

*Dr. S. Saleh, Dr. S. Daboss, T. Philipp, D. Schäfer, Prof. Dr. M. Rohnke, Prof. Dr. C. Kranz**

1 – 13

Probing the Properties of Locally Formed Solid Electrolyte Interphases on Hard Carbon Anodes